Available online at www.sciencedirect.com
SCIENCE DIRECT®
Pergamon
Acta Materialia 51 (2003) 6341–6357
Acta MATERIALIA
www.actamat-journals.com

A comparative study of precipitation behavior of Heusler phase (Ni_2TiAl) from B2-TiNi in Ni–Ti–Al and Ni–Ti–Al–X (X = Hf, Pd, Pt, Zr) alloys

J. Jung, G. Ghosh *, G.B. Olson

Department of Materials Science and Engineering, Robert R. McCormick School of Engineering and Applied Science, Northwestern University, 2220 Campus Dr., Evanston, IL 60208-3108, USA

Received 22 May 2003; received in revised form 30 July 2003; accepted 8 August 2003

Abstract

In support of the design of high strength TiNi-based shape-memory alloys, the precipitation of $L2_1$–Ni_2TiAl phase from a supersaturated $B2$–TiNi matrix at 600 and 800 °C is studied using transmission and analytical electron microscopy (TEM/AEM), and 3D atom-probe microscopy (3DAP) in Ni–Ti–Al and Ni–Ti–Al–X (X = Hf, Pd, Pt, Zr) alloys. A $B2/L2_1$ fully coherent two-phase microstructure is confirmed to be analogous to the classical γ/γ' system in terms of precipitate shape, spatial distribution and a minimum distance of separation between $L2_1$ precipitates as dictated by the interplay between strain and interfacial energies. The effects are also confirmed to disappear with loss of coherency. These results lend further support, at least qualitatively, to the theoretical predictions of microstructural dynamics of coherent aggregates. Selected cohesive properties of stable and virtual $B2$ compounds are calculated by an *ab initio* method, showing good agreement with measured site occupancy and lattice parameters. A simple analysis of the $L2_1$ precipitate size evolution suggests that in the case of alloys with Al, Zr or Hf substitution for Ti, the precipitates follow coarsening kinetics at 600 °C and growth kinetics at 800 °C, while for alloys with Pd or Pt substitution for Ni, precipitates follow one kinetic behavior at both temperatures. The temperature-dependent partitioning behaviors of Hf, Pd, Pt and Zr are established by quantitative microanalysis using AEM and nanoscale analysis using 3DAP. Both Hf and Zr prefer to partition to the $B2$ phase at 800 °C while they exhibit reverse behavior at 600°C. Pt also partitions to $B2$ at 800 °C, while Pd partitions to the $L2_1$ phase at both 600 and 800 °C. To describe the composition dependence of the lattice parameter of multicomponent $B2$ and $L2_1$ phases, the atomic volumes of Al, Hf, Ni, Ti and Zr in $B2$ and $L2_1$ phases are determined, providing a model for the control of interphase misfit in alloy design.

Keywords: 3DAP; *Ab initio* electron theory; Analytical electron microscopy; Heusler phases; Intermetallic phases; Kinetics; Precipitation

1. Introduction

The shape-memory effect is caused by a thermoelastic martensitic transformation—a reversible transformation between two different crystalline microstructures that occurs when a shape-memory alloy (SMA) is heated or cooled. An SMA is deformed in the martensite condition, and the shape recovery occurs during heating when the specimen undergoes a reverse transformation of the martensite to the parent phase. Under constrained conditions, the output stress during rever-

* Corresponding author. Tel.: +1-847-467-2595; fax: +1-847-491-7820.
E-mail address: g-ghosh@northwestern.edu (G. Ghosh).

1359-6454/$30.00
doi:10.1016/j.actamat.2003.08.003

sion is limited by the flow strength of the parent phase. For engineering applications, it is also essential that the shape-memory behavior is repeatable and predictable after many cycles through the transformation.

To improve both the output force and the cyclic lifetime of TiNi-based SMAs, the strength of the alloy must be improved. By raising the critical shear stress for slip, the irreversible slip deformation during the martensite reorientation and stress-induced martensite transformation can be suppressed, which in turn improves the shape memory effect and transformation superelasticity characteristics [1]. The introduction of nanoscale second phase particles to serve as barriers to dislocation motion would also improve the fatigue life. Based on the structural analogy of fcc-based γ/γ' Ni superalloys, the precipitation of equilibrium Heusler phase (Ni_2TiAl-type with $L2_1$ structure) in $B2$–TiNi is considered for strengthening in the present work. Koizumi et al. [2] previously demonstrated that the precipitation of Heusler phase increases the 0.2% compressive yield strength of a stable 50.71Ni–40.86Ti–8.43Al (in at.%) alloy by an order of magnitude up to 2300 MPa. Another precipitation strengthening method involves the formation of a metastable bct phase [3,4]. However, so far, this strategy has been realized only during the annealing of sputter deposited TiNi thin films.

According to the known lattice constants [5], there is a lattice misfit between TiNi and Ni_2TiAl, as determined by the relation

$$\delta = \left(\frac{a_{Ni_2TiAl} - 2a_{TiNi}}{2a_{TiNi}}\right) = -0.0257 \qquad (1)$$

where a_{Ni_2TiAl} is the lattice parameter of Ni_2TiAl (a = 0.5865 nm) and a_{TiNi} is the lattice parameter of TiNi (a = 0.3010 nm). Lattice misfit arising from different lattice parameters between two coherent phases causes coherency strains with an associated volume strain energy that can affect the precipitate shape, the spatial distribution and the coarsening behavior [6]. To promote fine scale homogeneous precipitation, to retain coherency at larger particle size and to reduce the interfacial frictional work for martensite nucleation and variant growth, it is necessary to minimize the lattice mismatch. To achieve the lowest possible misfit between $B2$ and $L2_1$ phases, the possibility of increasing the lattice parameter of the latter phase by adding Hf, Pd, Pt, or Zr in the alloy is considered.

It is well known that dissolved Al in $B2$–TiNi decreases the martensite start temperature drastically [7]. To offset this effect, elements which can stabilize the martensite phase will have to be added. In this regard, Hf, Zr, Pd, and Pt are candidate components as they are known as martensite stabilizers and also effective in reducing the lattice misfit between the $B2$ and $L2_1$ phase [8–11]. However, to control misfit and martensite stability in such a two-phase system, it is necessary to know the relative partitioning behavior that is established during high temperature heat treatment [12].

In the present work, the $B2$–$L2_1$ phase relations are quantified in Ni–Ti–Al and Ni–Ti–Al–X (X = Hf, Pd, Pt, Zr) model alloys. The primary objectives of this study are: (i) to investigate precipitation kinetics and microstructure evolution of $L2_1$ precipitates in a $B2$ matrix during isothermal aging at 600 and 800 °C, (ii) to quantify partitioning behavior of Hf, Pd, Pt and Zr between $B2$ and $L2_1$ at 600 and 800 °C, and (iii) to develop and test the composition dependence of the lattice parameters of multicomponent $B2$ and $L2_1$ phases.

2. Experimental procedures

Ni–Ti–Al and Ni–Ti–Al–X (X = Hf, Pd, Pt, Zr) alloys were prepared by arc-melting in an argon atmosphere using pure elements (99.98–99.994 wt.% Ni, 99.99 wt.% Ti, 99.999 wt.% Al, 99.9 wt.% Hf, 99.98 wt.% Pd, 99.95 wt.% Pt, and 99.999 wt.% Zr). The nominal chemical compositions of each of these alloys are shown in Table 1. Taking equiatomic TiNi as a reference, in alloys A, A + 5Hf and A + 5Zr, the Ni-content was kept at 50 at.%, while Ti was partially replaced by Al, Hf or Zr. On the other hand, in alloys B + 5Pd, B + 20Pd and B + 5Pt, Ni was partially substituted by Pd and Pt.

Each as-cast specimen was sealed in an evacuated quartz capsule and solution treated at 1100 °C for 100 h. After quenching by crushing the cap-

Table 1
Nominal chemical composition of alloys (at.%)

Alloys	Ni	Ti	Al	Hf	Zr	Pd	Pt
A	50	45	5	–	–	–	–
A + 5Hf	50	40	5	5	–	–	–
A + 5Zr	50	40	5	–	5	–	–
B + 5Pd	45	44	6	–	–	5	–
B + 20Pd	30	44	6	–	–	20	–
B + 5Pt	45	44	6	–	–	–	5

sules in oil, different sets of A, A + 5Hf, and A + 5Zr specimens were annealed at 800 °C for 1000 h and at 600 °C for 1000 and 2000 h in evacuated quartz capsules, and then quenched into oil. Samples of B + 5Pd, B + 20Pd, and B + 5Pt specimens were annealed at 800 or 600 °C for 100 h in evacuated quartz capsules, and then quenched into oil. Although binary TiNi alloys are typically aged at 550 °C for 1 h to produce metastable Ni_4Ti_3 particles [13], in the present work, the specimens are aged for a prolonged time to grow the Heusler phase precipitates sufficiently large for the composition analysis. Thin foils for transmission electron microscopy (TEM) observation were prepared by standard twinjet electropolishing using a solution of 20% perchloric acid in 80% methanol as electrolyte at −40 to −50 °C.

Conventional transmission electron microscopy (CTEM) was performed in a Hitachi H8100 microscope operated at 200 kV. The centered dark-field TEM micrographs were scanned and the projected area of the $L2_1$ precipitates was measured on a Macintosh computer using the public domain NIH Image program [14]. Based on these measurements, the average equivalent spherical radius of the precipitates was derived.

For most specimens aged at 800 °C, the analytical characterization was performed in a Hitachi HF-2000 analytical electron microscope (AEM) equipped with an ultrathin-window Link energy dispersive X-ray (EDS) detector. The AEM was also operated at 200 kV. The take-off angle for the EDS detector was 68°. The X-ray collection time was 100 s and the electron probe size was about 8 nm. Care was taken to ensure that the particle being analyzed was not in a two-beam condition in order to minimize electron-channeling effects [15]. Background correction was done using the Desktop Spectrum Analyzer (DTSA 2.5.1) software [16].

The compositions of $B2$ and $L2_1$ phases in equilibrium at 800 °C were determined by analyzing the EDS data using a standard calibration method. The background-subtracted integrated intensities of the X-ray spectra were converted to compositions by the procedure described in Ref. [17]. X-ray spectra were collected from foils with a thickness of 100 nm or less. In this thickness range, Hf, Ni, Pd, Pt, Ti and Zr satisfied the criterion of a thin foil and the Cliff–Lorimer factor for Al was determined using the extrapolation method [18] due to the strong thickness dependence.

The compositions of $B2$ and $L2_1$ phases were determined by analyzing about 30 EDS spectra for each. The statistical accuracy of the composition determination is primarily limited by the counting statistics of the X-ray collection process [19]. The confidence interval is estimated by the statistics of the Student t-distribution. The relationship between the atomic fraction and the weight fraction was used to calculate the total relative error in the former from that in the latter using a standard mathematical procedure.

The Heusler precipitates formed at 600 °C are in general much too small compared to the foil thickness, and as a result, the EDS spectra would invariably contain some contribution from the matrix. Hence, the determination of exact composition of precipitates from EDS data would necessarily involve correction for the matrix overlap. To eliminate these uncertainties, a 3-dimensional atom-probe (3DAP) field-ion microscope was

employed to determine the composition of the phases in specimens aged at 600 °C. The 3DAP is equipped with a reflectron lens for energy compensated time-of-flight mass spectrometry. Field-ion microscopy tips were prepolished in a solution of 5–10 vol.% perchloric acid in butoxyethanol followed by an electropolishing in 2 vol.% perchloric acid in butoxyethanol. For field-ion imaging, 1×10^{-5} Pa Ne was used, and the tips were cooled to −213 °C. Atom-probe analyses were carried out at −213 °C at a pulse voltage-to-d.c. voltage ratio $f = 0.20$. The statistical error of 3DAP data is caused by the uncertainty due to counting statistics. The peaks were deconvoluted in reference to the natural isotope abundances to obtain correct compositions.

X-ray diffraction was performed using a Scintag machine with a copper target, excited to 40 kV and 20 mA. A step size of 0.01° and a counting time of 30 s per step were used for X-ray diffraction experiments. The X-ray diffraction peaks were deconvoluted by the MacDiff program [20], using a pseudo-Voigt method [21], to obtain the lattice parameter of $B2$ and $L2_1$ phases. High purity silicon powder was used as a standard for correcting the diffractometer misalignment.

3. Computational methodology

The formation energies of 11 $B2$ compounds relevant to the present study were carried out using the Vienna *ab initio* Simulation Package (VASP), the details of which are described elsewhere [22,23]. The VASP code is based on the electronic density functional theory. The VASP code implements Vanderbilt ultrasoft pseudopotentials [24], and uses iterative strategies based on residual minimization and preconditioned conjugate-gradient techniques for the diagonalization of the Kohn–Sham Hamiltonian. The energy cut-off for the plane-wave basis set was 314 eV.

For the Brillouin-Zone integration, Methfessel–Paxton [25] technique with a modest smearing of the one electron levels (0.1 eV) is used. The K-point mesh for Brillouin-Zone integration was constructed using the Monkhorst–Pack [26] scheme. A mesh of 20 × 20 × 20 was used, and the resulting formation energies are estimated to be numerically converged to a precision of about 1 meV/atom. For Ni and Ni-containing $B2$ phases, spin-polarized calculations are employed. All *ab initio* total energies are calculated at the generalized gradient approximation level to account for the non-locality of the exchange-correlation functional. Also, in this study, Ti-3*p* and Zr-4*p* states are treated as valence electrons.

4. Results

4.1. Phases and microstructure: CTEM

The presence/absence of Heusler phase in thin foils can be confirmed by examining the transmission electron diffraction pattern either along [1 1 0] or along [1 1 2] zone axis. Accordingly, the thin foils of as-quenched and aged specimens were always examined along or close to either of these zone axes.

Fig. 1 shows bright-field images of solution treated and quenched specimens. Fig. 1(d) shows large Ti_2Ni-based particles located on or near grain boundaries. These particles are preferentially etched by the electrolyte, which is consistent with the fact that Ti_2Ni is prone to corrosion [27]. Ti_2Ni melts at 984 °C [28], significantly lower than the solution temperature of 1100 °C. The morphology of these particles suggests that the Ti_2Ni-based phase existed as liquid droplets at the solution treatment, solidifying during the subsequent oil quenching. Fig. 1(e) shows a bright-field TEM micrograph of solutionized B + 20Pd specimen showing evidence of Heusler precipitates. However, Ti_2Ni-based particles were not observed. A very small size of the Heusler precipitates (<4 nm in diameter) in Fig. 1(e) suggests that precipitation occurred during quenching, and they were not present at the solution treatment temperature. On the other hand, the as-quenched B + 5Pt alloy does not exhibit Heusler precipitates.

Fig. 2(a) shows the [0 1 1] diffraction pattern that is observed in A, A + 5Hf, A + 5Zr, B + 5Pd, and B + 5Pt alloys, and it clearly shows the absence of any Heusler phase. On the other hand, the [0 1 1] diffraction pattern in Fig. 2(b), from

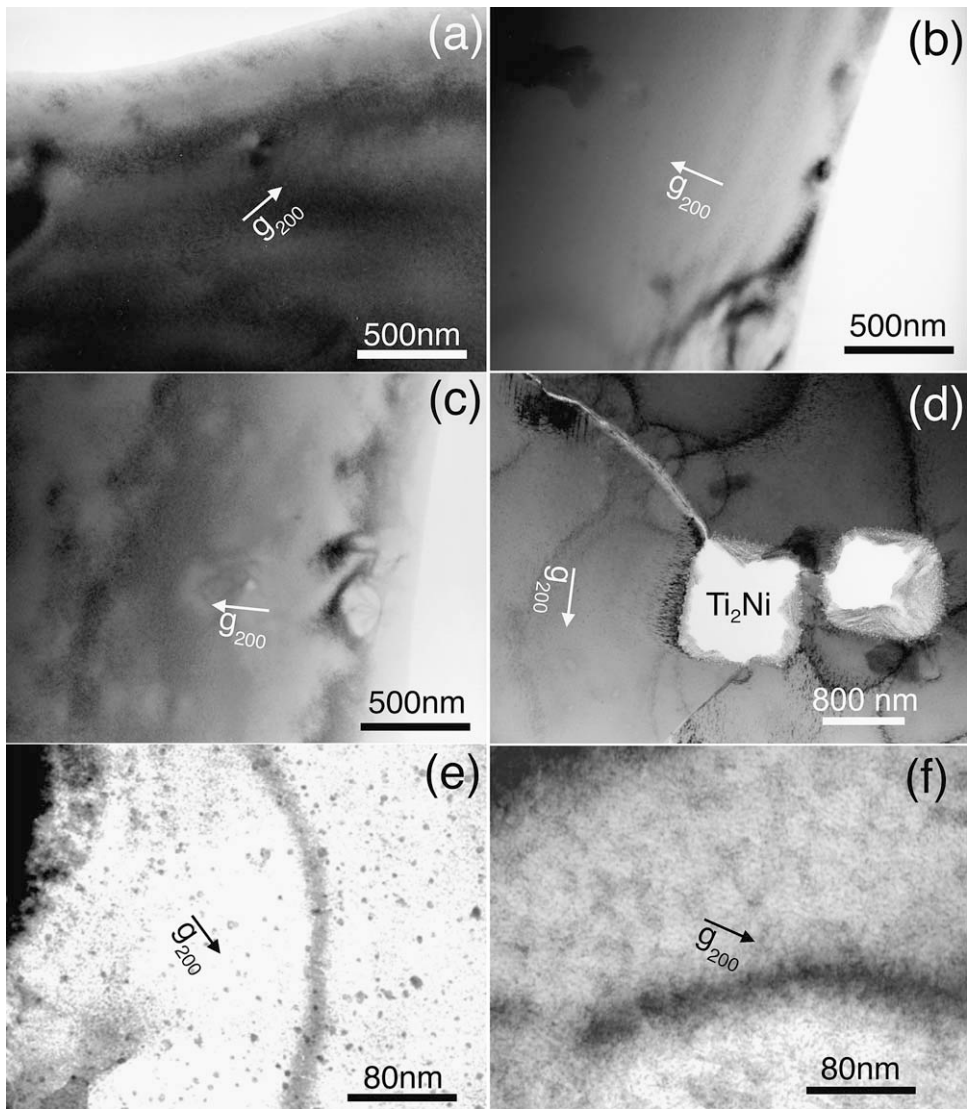

Fig. 1. Bright-field TEM micrographs of solutionized and as-quenched alloys (a) A, (b) A + 5Hf, (c) A + 5Zr, (d) B + 5Pd, (e) B + 20Pd, and (f) B + 5Pt. (d) shows the presence of Ti_2Ni-based particles. The presence of Heusler phase in (e) may be noted.

alloy B + 20Pd, shows superlattice reflection spots specific to the Heusler phase. This is consistent with very fine (~4 nm) $L2_1$ precipitates seen in Fig. 1(e).

Fig. 3 shows dark-field images of Heusler precipitates in the specimens aged at 600 and 800 °C. Centered dark-field images are obtained by using the (1 1 1)-type superlattice reflection specific to Heusler ordering. A representative [0 1 1] diffraction pattern of the aged specimens is shown in Fig. 4. Fig. 3(a)–(d) corresponds to aging for 1000 h, and Fig. 3(e)–(h) corresponds to that for 100 h. In all alloys, the precipitates remain fully coherent when aged at 600 °C, and the maximum precipitate diameter is 25 nm. Also, in general, a strong dominance of the misfit strains in this two-phase aggregate is observed through (i) the cuboidal shape of $L2_1$ precipitates, (ii) a strong spatial correlation where the $L2_1$ precipitates align preferentially along the elastically soft $\langle 1\,0\,0\rangle$ directions of the

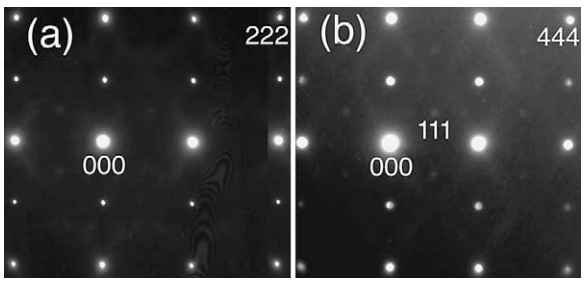

Fig. 2. [0 1 1] diffraction patterns of (a) A, A + 5Hf, A + 5Zr, B + 5Pd, and B + 5Pt and (b) B + 20Pd. (a) is indexed in terms of the $B2$ structure, while (b) is indexed in terms of the $L2_1$ structure. The diffraction pattern in (a) clearly demonstrates the absence of the $L2_1$ phase.

$B2$ matrix, and (iii) a minimum distance of separation. As anticipated, these features are remarkably analogous to the classical γ/γ' coherent microstructure [29]. It has been shown by extensive theoretical modeling that these features are dictated by a crucial interplay between strain and interfacial energies [30]. However, the extent of these effects is related to misfit strain, elastic anisotropy, and the volume fraction of the precipitate.

In the alloy B + 20Pd aged at 800 °C, two modes of Heusler precipitate sizes are observed, as shown in Fig. 3(f). The larger precipitates (mean diameter is about 150 nm) are the result of nucleation and growth of those formed during isothermal aging and also growth/coarsening of those formed during quenching from solution treatment temperature (see Fig. 1(e)). The smaller precipitates (≈5 nm in diameter) are believed to have formed during quenching from the aging temperature of 800 °C.

The $L2_1$ particles in the alloy B + 20Pd (see Fig. 3(f)) and in the alloy B + 5Pt (see Fig. 3(h)) are larger than the foil thickness so that the analytical electron microscopy can be conducted without inducing any matrix effect. On the other hand, the finer $L2_1$ precipitates in the alloy B + 5Pd needed to be analyzed with 3DAP microscopy. In Fig. 3(h), corresponding to alloy B + 5Pt, misfit dislocations are present at the precipitate/matrix interfaces indicative of a large lattice misfit. This is in contrast to the alloy B + 20Pd (see Fig. 3(f)) where large spherical precipitates without misfit dislocations, indicative of low lattice misfit, are observed.

The mean value of the precipitate radius, $\overline{r}$, and the width of the particle size distribution as a function of aging time and temperature are given in Table 2. It is important to note that in alloys A, A + 5Hf and A + 5Zr, $\overline{r}$ at 800 °C is larger than at 600 °C by a factor of 41 or more, while in alloys B + 5Pd, B + 20Pd and B + 5Pt, $\overline{r}$ at 800 °C is larger than at 600 °C by a factor of less than 14. These results will be analyzed further to identify possible mechanisms governing the microstructural dynamics.

4.2. Partitioning behavior

4.2.1. Analytical electron microscopy

The k factors used in this study were $k_{Al/Ni}$ = 0.7043 ± 0.0143, $k_{Pd/Ni}$ = 2.2906 ± 0.2030, $k_{Pt/Ni}$ = 1.7771 ± 0.1435, and $k_{Ti/Ni}$ = 0.9810 ± 0.0104. Fig. 5 shows the EDS X-ray spectra of $B2$ and $L2_1$ obtained from (a) A, (b) A + 5Zr, and (c) B + 5Pt aged at 800 °C. The qualitative difference in composition is clearly visible in the Al peak. The compositions of $B2$ and $L2_1$ phases are listed in Table 3.

The partition coefficients ($\kappa_x^{B2/L2_1} = x^{B2}/x^{L2_1}$) of Hf, Pd, Pt, and Zr at 800 °C are determined based on the AEM data to be 2.17 for Hf, 0.68 for Pd, 2.17 for Pt, and 1.35 for Zr. Hf, Pt, and Zr show a preference to partition to the $B2$ phase at this temperature. This weakens their effectiveness in reducing the lattice misfit. However, the stabilization of the martensite phase can be expected, allowing a higher transformation temperature [8–11]. The addition of Pd to the TiNi–Ni_2TiAl system is amenable for lattice misfit reduction, as manifested in the spherical precipitates of Fig. 3(f).

The Heusler precipitates in all specimens aged at 600 °C and B + 5Pd aged at 800 °C are too small to conduct AEM experiments using thin foil specimens without having to consider matrix overlap in the quantitative analysis of data. To overcome these difficulties, the higher resolution 3DAP technique was employed to determine the compositions of $B2$ and $L2_1$ phases in these microstructures.

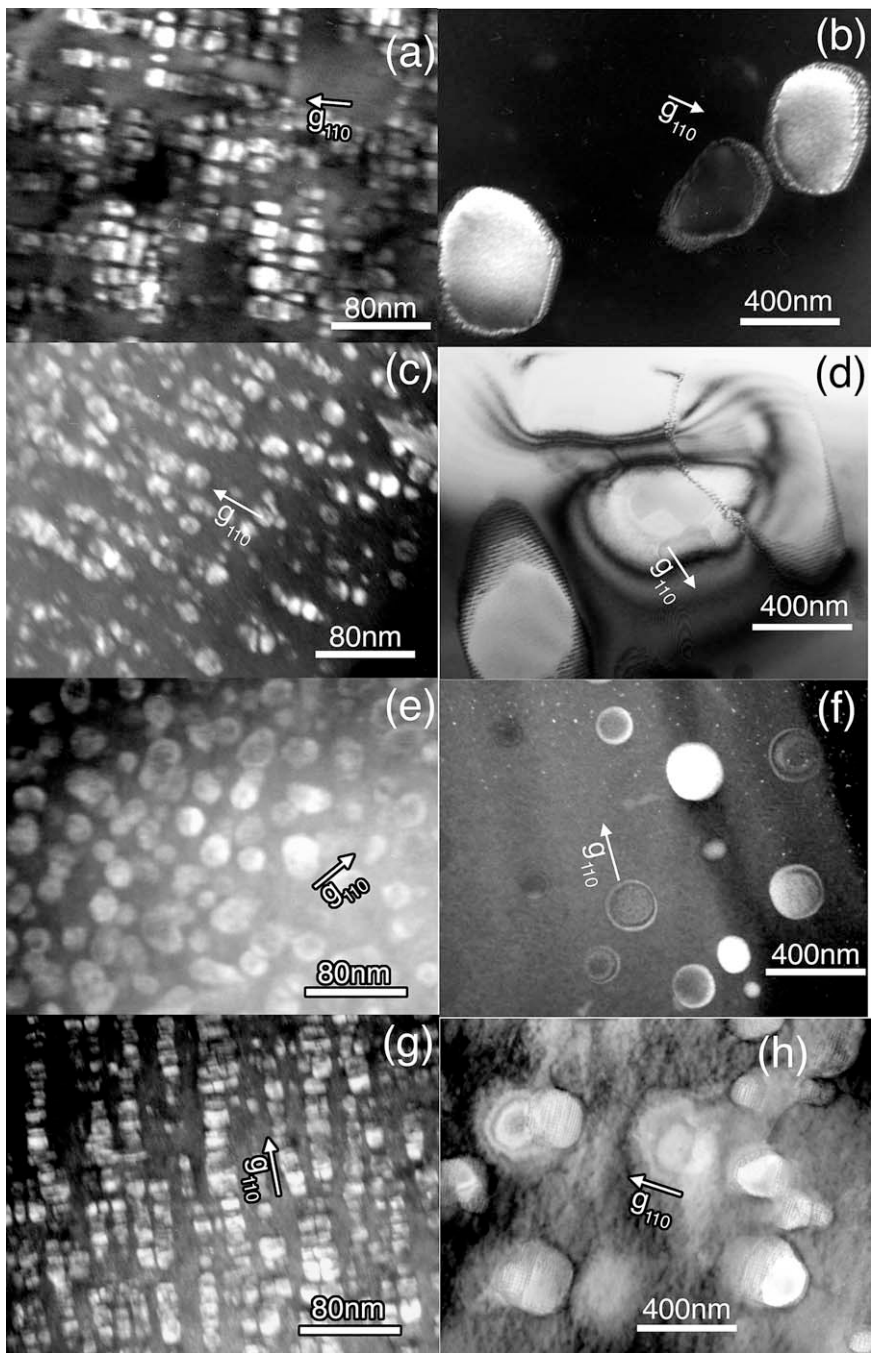

Fig. 3. Dark-field TEM micrographs of specimens aged at 600 (a, c, e, g) and 800 °C (b, d, f, h) showing fully coherent Heusler precipitates: (a–b) alloy A, (c–d) alloy A + 5Zr, (e–f) alloy B + 20Pd, (g–h) alloy B + 5Pt. Aging time for (a–d) is 1000 h, and for (e–h) it is 100 h.

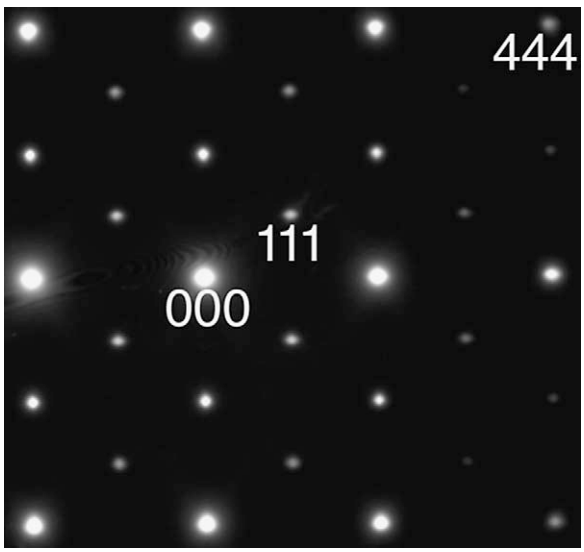

Fig. 4. [0 1 1] diffraction pattern of alloy A aged at 600 °C for 1000 h. Diffraction pattern is indexed in terms of the $L2_1$ structure.

4.2.2. 3D atom-probe microscopy

The average compositions, based on 3DAP analysis, of the phases observed during aging at 600 °C and B + 5Pd aged at 800 °C are listed in Table 4. The partitioning coefficient of Hf and Zr at 600 °C is $\kappa_{\mathrm{Hf}}^{B2/L2_1} = 0.87$, and that of Zr is $\kappa_{\mathrm{Zr}}^{B2/L2_1} = 0.75$, showing inversion of partitioning compared to 800 °C. The partitioning coefficient of Pd at 800 °C is $\kappa_{\mathrm{Pd}}^{B2/L2_1} = 0.64$, and at 600 °C, it is $\kappa_{\mathrm{Pd}}^{B2/L2_1} = 0.60$ or 0.53 for B + 5Pd and B + 20Pd, respectively. This shows that the partitioning coefficient of Pd is virtually independent of the temperature and composition, in contrast to Hf or Zr which shows a temperature sensitive partitioning behavior. B + 5Pt could not be analyzed because no suitable electrolyte was found for specimen preparation.

Ti_2Ni_3-based particles are found in A + 5Hf and A + 5Zr aged at 600 °C. The metastable Ti_2Ni_3 phase composition shows strong partitioning of Hf and Zr toward this phase. Both A + 5Hf and A + 5Zr were slightly Ni rich, and the Ti_2Ni_3 phase should be avoidable in a Ni lean alloy composition.

4.3. Lattice parameter measurements by X-ray diffraction and atomic volumes

The composition dependence of lattice parameter in *B*2–TiNi can be described in terms of site fractions of the species. In other words, the volume of the unit cell is the weighted sum of the species (including constitutional vacancies)

$$a^3 = \sum_{j=1}^{n} (y_j^{\mathrm{Ni}} + y_j^{\mathrm{Ti}})\Omega_j^{\mathrm{TiNi}} \tag{2}$$

with $\Sigma y_j^{\mathrm{Ni}} = \Sigma y_j^{\mathrm{Ti}} = 1$, where the superscripts Ni and Ti refer to two sublattices. The lattice parameter for the Heusler phase can also be described in terms of site fractions of the species as in the *B*2 system. Knowing the atomic volume of all species and their site occupancies on the sublattices of the Heusler structure, the lattice parameter in the multicomponent system can be modeled as follows:

$$a^3 = \sum_{j=1}^{n} (8y_j^{\mathrm{Ni}}\Omega_j^{\mathrm{Ni_2TiAl}} + 4y_j^{\mathrm{Ti}}\Omega_j^{\mathrm{Ni_2TiAl}} + 4y_j^{\mathrm{Al}}\Omega_j^{\mathrm{Ni_2TiAl}}) \tag{3}$$

By determining the atomic volumes of Al, Hf, Ni, Ti, Pd, Pt, and Zr in *B*2–TiNi and $L2_1$ phases, the

Table 2
Average radius $\bar{r}$ (nm) of Heusler precipitates, with the width of the particle size distribution. The number of precipitates used in each measurement is given in parentheses. The alloys A, A + 5Hf, and A + 5Zr are aged for 1000 h, while B + 5Pd, B + 20Pd, and B + 5Pt are aged for 100 h

Aging treatment (°C)	A	A + 5Hf	A + 5Zr	B + 5Pd	B + 20Pd	B + 5Pt
600	7.50 ± 1.97 (176)	6.24 ± 1.53 (50)	5.65 ± 1.00 (50)	9.48 ± 1.54 (50)	12.7 ± 2.38 (50)	6.88 ± 1.24 (50)
800	332 ± 158 (50)	312 ± 105 (50)	233 ± 81.3 (50)	34.6 ± 5.04 (50)	75.5 ± 21.4 (50)	96.8 ± 34.8 (50)

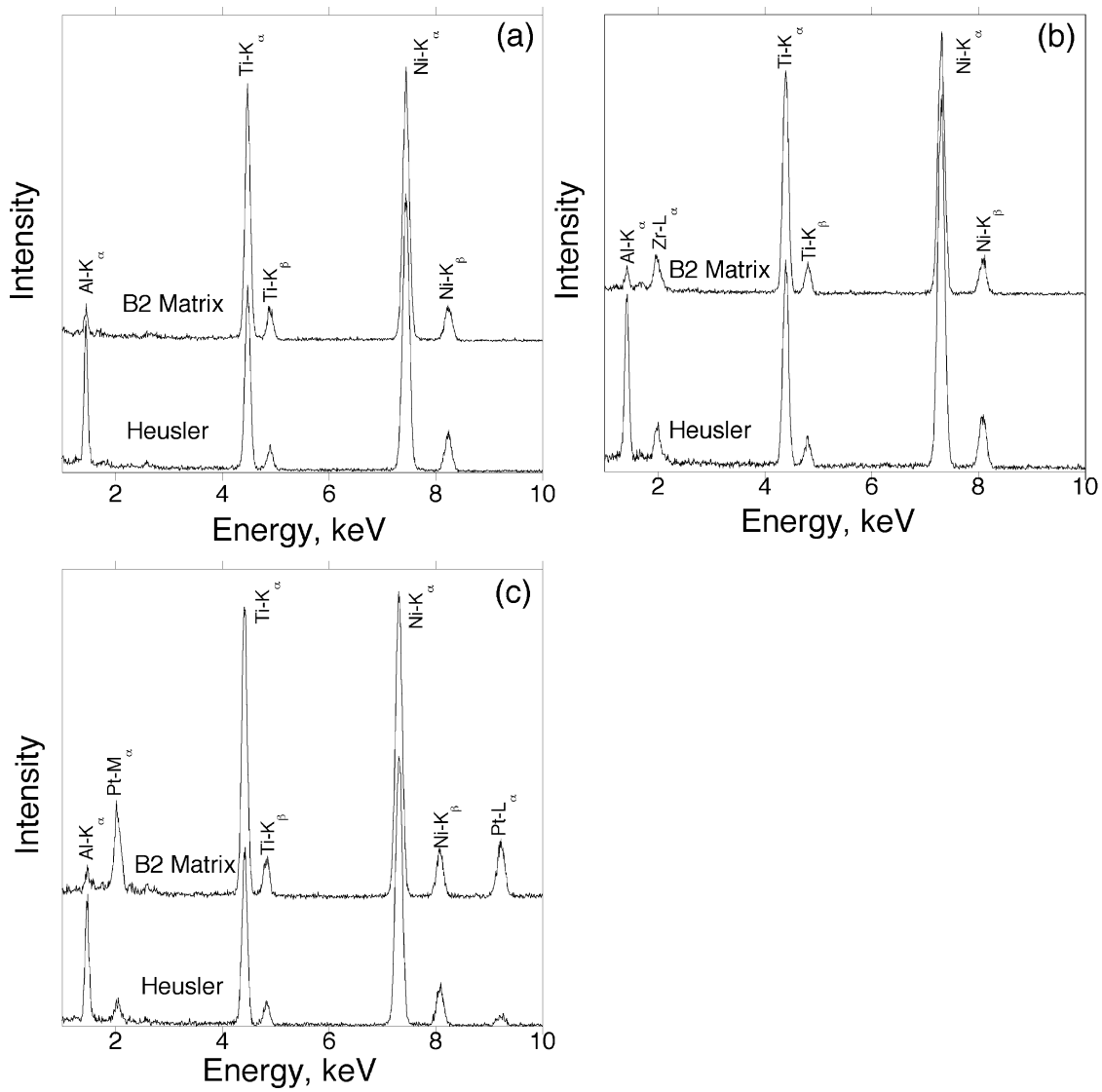

Fig. 5. An as-collected EDS X-ray spectrum from a *B*2 matrix and a semicoherent Heusler phase particle after aging (a) A, (b) A + 5Zr, and (c) B + 5Pt at 800 °C. The X-ray collection time was 100 s. Background correction was performed using DTSA software.

composition dependence of the lattice misfit between multicomponent *B*2 and $L2_1$ can be described.

The ambient lattice parameters of *B*2 and $L2_1$ phases obtained from the X-ray diffraction experiments, corrected for instrumental factors, are listed in Table 5 as a function of heat treatment. Lattice parameters for solutionized B + 5Pd and B + 20Pd are not listed because Ti_2Ni precipitates were observed in B + 5Pd and Heusler precipitation was not suppressed in B + 20Pd.

Using the experimental lattice parameters, the atomic volumes of Al, Ti, Ni, and Zr in both TiNi and Ni_2TiAl have already been reported [17]. Here, we derive the atomic volumes of Pd (Ω_{Pd}^{TiNi}) and Pt (Ω_{Pt}^{TiNi}). Ref. [11] reported the effect of Pd on the lattice parameter of TiNi. Using their data in conjunction with Eq. (2), we obtain Ω_{Pd}^{TiNi} = 0.0172

Table 3
Equilibrium compositions of *B*2 (TiNi) and Heusler (Ni_2TiAl) phases at 800 °C determined by AEM. The uncertainty refers to 99% confidence level

Alloy	Phase	Al (at.%)	Ti (at.%)	Ni (at.%)	Hf, Pd, Pt, or Zr (at.%)
A	*B*2	3.80±0.17	43.15 ± 0.35	53.04	–
	Heusler	19.79±0.74	27.94 ± 0.09	52.27	–
A + 5Hf	*B*2	4.13±0.39	38.65 ± 0.09	51.75	5.48±0.31
	Heusler	20.52±0.84	25.23 ± 0.12	51.72	2.53±0.17
A + 5Zr	*B*2	3.91±0.27	39.77 ± 0.17	51.14	5.18±0.27
	Heusler	21.80±0.66	23.80 ± 0.02	50.56	3.84±0.21
B + 20Pd	*B*2	4.13±0.24	43.47 ± 0.75	29.02	23.38±2.06
	Heusler	15.70±0.22	28.13 ± 0.83	21.54	34.63±2.50
B + 5Pt	*B*2	2.93±0.28	45.67 ± 0.01	45.89	5.50±0.88
	Heusler	20.52±1.04	30.48 ± 0.30	49.45	2.53±0.24

Table 4
Compositions of the phases present as determined by 3DAP. The uncertainty refers to the $\pm 2\sigma$ interval in a binomial distribution

Alloy (°C)	Phase	Al (at.%)	Ti (at.%)	Ni (at.%)	Hf, Pd, Pt, or Zr (at.%)
A (600)	*B*2	2.67±1.10	44.29 ± 0.84	53.05 ± 0.76	–
	Heusler	23.54±1.84	26.02 ± 1.80	50.44 ± 1.48	–
A + 5Hf (600)	*B*2	2.14±0.54	44.32 ± 0.40	51.34 ± 0.38	2.20±0.54
	Heusler	16.56±1.22	27.89 ± 1.14	53.02 ± 0.92	2.52±1.32
	Ti_2Ni_3	2.17±3.08	31.20 ± 2.60	58.37 ± 2.02	8.26±3.00
A + 5Zr (600)	*B*2	2.28±2.06	43.68 ± 1.56	51.10 ± 1.46	2.94±2.06
	Heusler	21.70±2.32	26.96 ± 2.24	47.45 ± 1.90	3.90±2.58
	Ti_2Ni_3	0.00±0.00	24.41 ± 4.52	64.37 ± 3.10	11.22±4.90
B + 5Pd (800)	*B*2	4.69±1.14	42.30 ± 0.88	48.11 ± 0.84	4.90±1.14
	Heusler	21.24±4.08	29.13 ± 3.86	42.00 ± 3.50	7.63±4.42
B + 5Pd (600)	*B*2	2.80±1.10	44.50 ± 0.82	47.43 ± 0.80	5.27±1.08
	Heusler	22.04±1.92	28.97 ± 1.84	40.23 ± 1.68	8.76±2.08
B + 20Pd (600)	*B*2	2.54±2.36	46.47 ± 1.76	33.76 ± 1.94	17.23±2.18
	Heusler	21.36±1.14	29.42 ± 1.08	16.77 ± 1.18	32.46±1.06

Table 5
Lattice parameter of *B*2 phase in solution treated (at 1100 °C) alloys, and *B*2 and $L2_1$ phases in aged (at 800 or 600 °C) alloys

	Phase	A	A + 5Hf	A + 5Zr	B + 5Pd	B + 20Pd	B + 5Pt
Solution treated	*B*2	0.30018 nm	0.30331 nm	0.30543 nm	–	–	0.30059 nm
Aged at 800 °C	*B*2	0.30022 nm	0.30298 nm	0.30468 nm	0.30360 nm	0.30612 nm	0.30202 nm
	Heusler	0.59068 nm	0.59410 nm	0.59851 nm	0.60175 nm	0.61031 nm	0.58073 nm
δ at 25 °C		−0.0163	−0.0196	−0.0178	−0.0090	−0.0031	−0.0386
Aged at 600 °C	*B*2	0.30132 nm	0.30171 nm	0.30255 nm	0.30276 nm	0.30579 nm	0.30239 nm
	Heusler	0.59358 nm	0.59518 nm	0.60351 nm	0.59818 nm	0.60397 nm	0.59446 nm
δ at 25 °C		−0.0150	−0.0137	−0.0026	−0.0121	−0.0124	−0.0171

nm^3. As there are no literature lattice parameter data of $B2$ Ti(Ni,Pt) alloys, the lattice parameter of the solution treated B + 5Pt specimen was used as a reference, and we obtain Ω_{Pt}^{TiNi} = 0.0144 nm^3. The results are summarized in Table 6.

We have also derived the atomic volume of Pd and Pt in the $L2_1$ phase using the following approximations based on the substitution behavior described in Ref. [17]:

$$\Omega_{(Pd,Pt)}^{Ni_2TiAl} = \Omega_{(Pd,Pt)}^{TiNi} \times \frac{\Omega_{Ti}^{Ni_2TiAl}}{\Omega_{Ti}^{TiNi}} \quad (4)$$

However, the lattice parameter of $L2_1$ was systematically overestimated using this approximation. In the absence of any experimental lattice parameter data of single phase (Ni,Pd,Pt)$_2$TiAl alloys, the $L2_1$ lattice parameters of B + 20Pd and B + 5Pt aged at 800 °C were used as a reference in order to derive $\Omega_{Pd}^{Ni_2TiAl}$ = 0.0155 nm^3 and $\Omega_{Pt}^{Ni_2TiAl}$ = 0.0110 nm^3.

In the case of Hf or Zr substituting for Ti in $L2_1$, the atomic size effect associated with atomic cores can be determined as follows: $\Delta\Omega_{(Hf,Zr)} = (\Omega^*_{(Hf,Zr)} - \Omega_{Ti})/\Omega_{Ti}$ = +0.56 for Hf and +0.94 for Zr. In other words, Hf atoms are calculated to be 56% larger than the Ti atoms they replace, and Zr atoms are 94% larger. In the case of Pd or Pt substituting for Ni, $\Delta\Omega_{(Pd,Pt)} = (\Omega^*_{(Pd,Pt)} - \Omega_{Ni})/\Omega_{Ni}$ = +0.35 for Pd and −0.04 for Pt. This shows that for any given amount of substitution, Zr is most effective in increasing the lattice parameter of the $L2_1$ phase. Pt will not contribute in the reduction of the lattice misfit regardless of the partition behavior since $\Omega_{Pt}^{TiNi} > \Omega_{Ni}^{TiNi}$ but $\Omega_{Pt}^{Ni_2TiAl} < \Omega_{Ni}^{Ni_2TiAl}$. The small atomic volume of Pt in $L2_1$ suggests a strong bonding interaction between Pt and Ti, or Pt and Al.

Table 6
The atomic volumes (in nm^3) of Ni, Al, Ti, Hf, Pd, Pt, and Zr at 25 °C derived from the lattice parameter data of TiNi and Ni$_2$TiAl. These values are compared with atomic volumes in the respective stable reference state of the elements

Species	TiNi	Ni$_2$TiAl	Stable elemental state
Ni	0.0123	0.0115	0.0109 (fcc)
Al	0.0114	0.0124	0.0166 (fcc)
Ti	0.0151	0.0157	0.0177 (hcp) [31]
Hf	0.0236	0.0245	0.0224 (hcp) [32]
Pd	0.0172	0.0155	0.0147 (fcc) [33]
Pt	0.0144	0.0110	0.0151 (fcc) [33]
Zr	0.0293	0.0305	0.0233 (hcp) [34]

5. Discussion

5.1. Ab initio results and relevance to experimental data

Selected cohesive properties of the $B2$ phases relevant to the present study are listed in Table 7. Among the $B2$ phases, four (NiAl, TiNi, TiPd, TiPt) are stable, as they appear in the corresponding binary phase diagrams, and the others should be considered as virtual phases.

The heat of formation (ΔH_f) of the stable $B2$

Table 7
Ab initio heat of formation (ΔH_f) and lattice parameter of Ni–X and Ti–X $B2$ intermetallics

Phase	Reference state	Heat of formation (kJ/mol)	Lattice parameter (nm)
TiNi[a]	hcp-Ti, fcc-Ni	−35.730	0.30200
	bcc-Ti, fcc-Ni	−40.900	
NiAl[b]	fcc-Al, fcc-Ni	−63.411	0.28961
NiHf	hcp-Hf, fcc-Ni	−42.940	0.31673
	bcc-Hf, fcc-Ni	−50.760	
NiPd	fcc-Ni, fcc-Pd	+6.513	0.29982
NiPt	fcc-Ni, fcc-Pt	−0.928	0.29999
NiZr	fcc-Ni, hcp-Zr	−34.327	0.32223
	fcc-Ni, bcc-Zr	−37.767	
TiAl	fcc-Al, hcp-Ti	−25.826	0.31897
	fcc-Al, bcc-Ti	−30.996	
TiHf	hcp-Hf, hcp-Ti	+12.495	0.33916
	bcc-Hf, bcc-Ti	−0.495	
TiPd[c]	hcp-Ti, fcc-Pd	−43.979	0.31862
	bcc-Ti, fcc-Pd	−51.149	
TiPt[d]	hcp-Ti, fcc-Pt	−77.286	0.31918
	bcc-Ti, fcc-Pt	−82.455	
TiZr	hcp-Ti, hcp-Zr	+10.150	0.34252
	bcc-Ti, bcc-Zr	+1.541	

Previous *ab initio* prediction based on ground states:
[a] TiNi: −35.7 to –52.0 kJ/mol [36,39].
[b] NiAl: –63 to –80 kJ/mol [35].
[c] TiPd: –61 to –97 kJ/mol [36].
[d] TiPt: –69.3 kJ/mol [40].

phases has been investigated, both experimentally and theoretically. Our calculated ΔH_f is in good agreement with the reported calorimetric measurements as well as previous *ab initio* results. In the case of NiAl, both calorimetric data and theoretical predictions are critically assessed by Rzyman et al. [35]. Experimental ΔH_f for NiAl lies between -58.3 ± 1.1 to -67.4 ± 2.55 kJ/mol, and our predicted value of -63.411 kJ/mol is well within the range of experimental values. In the case of TiNi, our predicted ΔH_f is -40.9 kJ/mol with respect to bcc-Ti and fcc-Ni. The experimental ΔH_f is -34.0 ± 2.0 kJ/mol [36], measured at 1202 °C. ΔH_f values of -31.6~-33.9 have been reported previously [36]; however the temperature was not well documented. The predicted ΔH_f is overestimated by more than 5 kJ/mol. The predicted ΔH_f of TiPd and TiPt are -51.149 and -82.455 kJ/mol. The experimental values -53.1 ± 3.0 kJ/mol for TiPd measured at 1250 °C [36], and -77.1 ± 3.1 kJ/mol for TiPt measured at 1400 °C [36] demonstrate good agreement.

Linear extrapolation of the temperature dependence of the lattice parameter of TiNi [37] gives $a = 0.30151$ nm at 0 K, which is in very good agreement with our predicted value of 0.3020 nm. For NiAl, we have used experimental data of Hughes et al. [38]. A non-linear least square fit yields $a = 0.28805$ nm at 0 K compared to the predicted value of 0.28961 nm, a discrepancy of only 0.5%. In the case of TiPd and TiPt, experimental data as a function of temperature are not available; thus a comparison could not be made with our predicted values.

The measured lattice parameters of solution treated and quenched ternary and quaternary *B*2 alloys are also consistent with the *ab initio* lattice parameter values. For example, ternary alloy A may be conceived as a mechanical mixture of 90 mol% TiNi and 10 mol% of NiAl. This yields a predicted lattice parameter of 0.30076 nm at 0 K, which compares favorably with the lattice parameter value of 0.30018 nm at room temperature (see Table 5). Similarly, the lattice parameters of A + 5Hf and A + 5Zr can be calculated with the *ab initio* lattice parameter values, where A + 5Hf is approximated as 80 mol% TiNi + 10 mol% NiAl + 10 mol% NiHf, and A + 5Zr as 80 mol% TiNi + 10 mol% NiAl + 10 mol% NiZr. Incorporating the temperature dependency of lattice parameter, the calculated lattice parameters are 0.30278 and 0.30333 nm, respectively. Compared to the experimental data of Table 5, they show a discrepancy of less than 0.7%.

Another important *ab initio* result is the ability to predict site occupancy of Hf and Zr in the *B*2 phase. Earlier, we had reported experimental determination of site occupancy of Hf and Zr in *B*2 of alloys A + 5Hf and A + 5Zr aged at 600 °C. This was done by atomic scale chemical analysis of (1 0 0) layers in a 3DAP [17]. The results are summarized in Table 8 [17]. The site occupancy of Pd and Pt in *B*2 could not be measured due to experimental difficulty. Nevertheless, we find that more than 80% of Hf and Zr atoms in *B*2 phase reside on the Ti-sublattice. This is expected from the trends of ΔH_f values of NiHf, NiZr, TiHf, and TiZr. When Hf or Zr atoms reside on the Ti-sublattice, they form Ni–Hf and Ni–Zr nearest neighbor bonds which are energetically more favorable compared to the formation of Ti–Hf and Ti–Zr nearest neighbor bonds when Hf and Zr reside on the Ni-sublattice. While the vast majority of the site occupancy is consistent with the enthalpic criterion alone, some intermixing is expected at finite temperature due to configurational entropy.

5.2. Kinetics of $L2_1$ precipitation

In order to predictively control desired nanoscale microstructure, it is of fundamental importance to investigate the microstructural dynamics that determines the characteristic length scales of the precipitates. It is well established that the kinetics of precipitation from a supersaturated solid solution is governed by the interplay of three pro-

Table 8
Experimental site occupancy of Hf and Zr in *B*2 and $L2_1$, as determined by 3DAP[17]

	Site	Hf ± 2σ	Zr ± 2σ
*B*2	Ti	82 ± 8%	83 ± 10%
$L2_1$	Ti	89 ± 20%	83 ± 30%

cesses: (i) nucleation of precipitates, (ii) their growth kinetics, and (iii) coarsening (or Ostwald ripening) of the precipitates. Even though the distinction between the growth and coarsening stages is somewhat arbitrary and these three processes may overlap, we seek to identify the governing processes at 600 and 800 °C. Of particular interest is the competition between growth and coarsening.

As shown in Fig. 1, the nucleation of $L2_1$ precipitates was suppressed during quenching following solution treatment in all alloys except B + 20Pd. Therefore, all three processes may take place during isothermal aging in these alloys, while some nucleation has occurred in B + 20Pd during oil quenching prior to aging which may continue further during isothermal aging along with growth and coarsening.

Since both growth and coarsening processes are diffusion controled, it is necessary to consider the diffusion data in the multicomponent $B2$ phase. Unfortunately, the diffusion data for all relevant elements in $B2$–TiNi are not available, and therefore the slowest diffusing species cannot be identified. Available diffusion data for congruently melting $B2$ intermetallics [41–48], summarized in Table 9, show that the diffusivities of the components do not differ appreciably. From Table 9, it can be seen that the diffusivity ratio D_B/D_A in $B2$ compounds at the stoichiometric composition falls within the limits 0.5–2 prescribed by the six jump cycle [49] with the exception of PdIn at low temperatures. It has been proposed that in PdIn, the diffusivities of both alloy components are not directly correlated and the diffusion of Pd can be described by next neighbor jumps of Pd into single Pd vacancies, while the diffusion of In occurs by both the nearest and next nearest neighbor jumps [45].

In the binary $B2$–TiNi, diffusivity data are available on a limited basis. Determination of the diffusivities in this system was based on either the growth kinetics of TiNi-layer in diffusion couples or tracer diffusion experiments using ^{63}Ni. Bastin and Rieck [50] have derived interdiffusion coefficients and diffusion activation energies using various diffusion couples to be $D_0 = 2.0 \times 10^{-9}$ m^2/s and $Q = 142$ kJ/mol, respectively. The variance of the activation energy over the composition range of 50–52 at.% Ni is less than the error of the measurement. This gives the volume interdiffusivity ($\tilde{D}^v$) of TiNi at 600 and 800 °C to be 6.37×10^{-18} and 2.44×10^{-16} m^2/s, respectively. In this case, $\tilde{D}^v_{800}/\tilde{D}^v_{600}$ is about 38.3.

Erdelyi et al. [51] measured the tracer diffusivity of ^{63}Ni in TiNi and observed Arrhenius behavior with $D_0 = 2.1 \times 10^{-9}$ m^2/s, $Q = 155.6$ kJ/mol. Bernardini et al. [52] reported consistent values through tracer volume diffusion measurements in the Ni–50.07at.%Ti binary and Ni–48.83at.%Ti–9.29at.%Cu ternary alloys. This gives the diffusivity (D^{Ni}) of ^{63}Ni in TiNi at 600 and 800 °C to be 1.03×10^{-18} and 5.59×10^{-17} m^2/s, respectively. Here, $D^{Ni}_{800}/D^{Ni}_{600}$ is about 54.3. Based on the data provided in Table 9, it is assumed that $D^{Ti}_{800}/D^{Ti}_{600}$

Table 9
A comparison of the diffusivities (D_A and D_B) in congruently melting $B2$ compounds at the stoichiometric composition as a function of normalized temperature ($T_H = T/T_M$). The aging temperatures 600 and 800 °C correspond to $T_H = 0.55$ and $T_H = 0.68$ in equiatomic TiNi. The T_M of AuCd, AuZn, PdIn, NiAl and NiGa is taken as 629, 758, 1285, 1638, and 1220 °C, respectively

Compound AB	Normalized temperature T_H							
	0.55			0.68			D''_A/D'_A	D''_B/D'_B
	D'_A	D'_B	D'_B/D'_A	D''_A	D''_B	D''_B/D''_A		
AuCd [42,43]	8.16×10^{-14}	9.97×10^{-14}	1.22	1.61×10^{-11}	2.01×10^{-11}	1.25	197.3	201.6
AuZn [44]	5.40×10^{-14}	4.08×10^{-14}	0.76	1.30×10^{-11}	1.44×10^{-11}	1.11	240.7	352.9
PdIn [45]	3.81×10^{-15}	4.70×10^{-14}	12.34	2.17×10^{-12}	5.52×10^{-12}	2.54	569.6	117.4
NiAl [46,47]	2.25×10^{-15}	1.93×10^{-15}	0.86	1.59×10^{-12}	2.16×10^{-12}	1.36	706.7	1119.2
NiGa [48]	1.03×10^{-12}	4.95×10^{-13}	2.08	1.14×10^{-10}	2.69×10^{-11}	2.36	110.7	54.3

will not be too different from 54.3. In the following analysis, both $D^{Ni}_{800}/D^{Ni}_{600}$ and $\tilde{D}^{v}_{800}/\tilde{D}^{v}_{600}$ are used.

If the diffusion controled growth process is operating at both temperatures for the isochronal heat treatment,

$$\frac{\bar{r}_{800}}{\bar{r}_{600}} \approx \sqrt{\frac{D_{800}}{D_{600}}} \approx 7.4 \tag{5}$$

using D^{Ni} values. If the volume interdiffusivity is used, the right hand side of Eq. (5) yields a value of 6.2. Based on the measured $\bar{r}$ data for alloys A, A + 5Hf and A + 5Zr (see Table 1), $\bar{r}_{800}/\bar{r}_{600}$ is about 41–50 which is much bigger than the expected value of 6.2–7.4 from Eq. (5). On the other hand, the $\bar{r}_{800}/\bar{r}_{600}$ in alloys B + 5Pd, B + 20Pd and B + 5Pt (see Table 2), is 3.6, 6.0, and 14, respectively. These are much closer to the expected value of 6.2–7.4 based on TiNi diffusion data.

Since nucleation has occurred prior to aging in B + 20Pd, Eq. (5) is modified as follows:

$$\frac{\bar{r}^2_{800}-\bar{r}^2_{0,800}}{\bar{r}^2_{600}-\bar{r}^2_{0,600}} \approx \frac{D_{800}}{D_{600}} \approx 38.3 \sim 54.3 \tag{6}$$

where $\bar{r}_{0,800}$ and $\bar{r}_{0,600}$ are radii at the onset of growth. $\bar{r}_{0,800}$ is measured as 2.5 nm and assuming $\bar{r}_{0,600} = \bar{r}_{0,800}$, the left hand side of Eq. (6) yields 36.7. Again, B + 20Pd provides a value close to that calculated on the right hand side based on both $\tilde{D}^{v}$ and D^{Ni}, and therefore, the mechanism for the kinetics of precipitation can be interpreted as diffusion controled growth at both temperatures. While B + 5Pt could also be explained by Eq. (6), it is worth considering alternative mechanisms for clarification.

For an isochronal heat treatment, if a coarsening process operates at both temperatures,

$$\frac{\bar{r}_{800}}{\bar{r}_{600}} \approx \sqrt[3]{\frac{f_{800}}{f_{600}}\frac{\sigma_S}{\sigma_C}\frac{D_{800}}{D_{600}}} \tag{7}$$

where the ratio f_{800}/f_{600} accounts for the effect of volume fraction on the coarsening rate constant, and σ_S and σ_C are the semicoherent and coherent interfacial energies. The difference in molar volume between 600 and 800 °C is ignored. Since the volume fraction of $L2_1$ decreases with increasing temperature, the ratio f_{800}/f_{600} will be always less than unity. Assuming $\sigma_S = 5\sigma_C$, and $f_{800}/f_{600} = 1$ as an upper limit, an upper bound value for the right hand side of Eq. (7) is evaluated as 5.76 based on $\tilde{D}^{v}$ and 6.47 based on D^{Ni}. These values are again much smaller than experimental $\bar{r}_{800}/\bar{r}_{600}$ in alloys A, A + 5Hf, A + 5Zr, but closer to those in alloys B + 5Pd, B + 20Pd and B + 5Pt.

If the growth process is operating at 800 °C while coarsening at 600 °C,

$$\frac{\bar{r}_{800}}{\bar{r}_{600}} \approx \frac{(X^{1100}_{B2}-X^{800}_{B2})/(X^{800}_{H}-X^{800}_{B2})\sqrt{D_{800}t}}{\sqrt[3]{8D_{600}\sigma_C t V_m X^{600}_{B2}(1-X^{600}_{B2})/(9RT(X^{600}_{H}-X^{600}_{B2})^2)}},$$

$$V_m = N_A\frac{a^3}{16} \tag{8}$$

where X^{1100}_{B2} is the concentration of Al in the solution treated specimen, X^{800}_{B2} and X^{600}_{B2} the concentrations of Al in $B2$ of the specimens aged at 800 and 600 °C, respectively, X^{800}_{H} and X^{600}_{H} the concentrations of Al in Heusler phase of the specimens aged at 800 and 600 °C, respectively. These are listed in Tables 3 and 4. R is the gas constant, T the temperature in K, V_m the average molar volume of the Heusler phase, N_A Avogadro's number and a the lattice parameter of Heusler phase at 600 °C. The concentration of Al is chosen because Al is the solute which undergoes the largest partitioning between the phases. Assuming a reasonable value for the coherent interfacial energy σ_C = 20 mJ/m^2, we find that $\bar{r}_{800}/\bar{r}_{600}$ lies in the range of 30.5–45.0 based on D^{Ni}, and 23.6–51.0 based on $\tilde{D}^{v}$. This is certainly much closer to the experimental $\bar{r}_{800}/\bar{r}_{600}$ values (41–50, see Table 2) in alloys A, A + 5Hf and A + 5Zr than the two other possible dynamics discussed, but much bigger than the experimental $\bar{r}_{800}/\bar{r}_{600}$ value in alloys B + 5Pd, B + 20Pd, and B + 5Pt.

It is well established that the splitting of precipitation kinetics into three distinct regimes is somewhat artificial, and in reality, all three processes may overlap. To address this issue, Langer and Schwartz [53] developed a general theory of precipitation kinetics where an important parameter is the degree of supersaturation. At high supersaturation, the nucleation rate is very high causing the supersaturation to drop rapidly. The decrease in supersaturation causes the particles smaller than

critical size to dissolve. The average particle size is initially governed by the nucleation process and smoothly changes to the regime governed by coarsening. The growth stage is bypassed because all the supersaturation is consumed during nucleation and coarsening. This seems to be the operating process at 600 °C in alloys A, A + 5Hf and A + 5Zr. On the other hand at low supersaturation, the precipitation kinetics proceeds through distinct stages of growth and coarsening. This may be the operating mechanism at 800 °C in alloys A, A + 5Hf and A + 5Zr, where the Al supersaturation ratio is decreased by 60% based on our measured tie lines. In contrast, the microstructural dynamics in alloys B + 5Pd, B + 20Pd and B + 5Pt can be described either by growth or by coarsening at both temperatures.

To account for the difference observed in the precipitation mechanisms of alloys A vs. B, the manifold assumptions made have to be validated carefully. Here, the microstructural dynamics in all alloys is discussed considering the TiNi diffusion data only, and no attempt was made to identify the slowest diffusing species in ternary and quaternary alloys. As seen in Table 9, the diffusivity of alloy components in $B2$ at a given temperature can differ significantly if the diffusion mechanisms are different as is the case for PdIn. As in random solid solutions, vacancies also mediate diffusion processes in $B2$ compounds. However, in ordered compounds, random vacancy motion is not possible, as it would disrupt the equilibrium ordered arrangement of atoms on sublattice sites. Furthermore, the degree of long-range order has a strong influence in $B2$ compounds which can be affected by the deviation from ideal stoichiometry. In a perfectly ordered state, the diffusion is much more sluggish compared with the case when the long-range order parameter is less than 1. A significant deviation from the highly ordered state can lead to a change in diffusion process from a six jump cycle mechanism to a triple defect mechanism [54]. Such a change in mechanism leads to a large disparity in D_A and D_B. Besides long-range order, solute-vacancy binding energy associated with various alloying elements can also exert significant influence on the diffusion kinetics.

A major difference between the alloys A and B is that in the former, the solutes (Al, Hf, or Zr) primarily reside on the Ti-sublattice, while in B, the solutes (Al, Pd or Pt) reside on both sublattices. This might have contributed to a decrease in long-range order parameter in B, thus accelerated diffusion kinetics. There are no solute diffusion data in TiNi base alloys, nor are there any theoretical guidelines to estimate the solute-vacancy binding energy, vacancy migration energy, etc. Both experimental and theoretical data for diffusion in TiNi are needed to fully interpret and understand the phase transformation kinetics in TiNi-based alloys.

To make TiNi-based shape-memory alloys strengthened by Heusler phase amenable to engineering applications, the $B2$ matrix must transform to martensite near or above room temperature. Calorimetric study of alloys after aging treatment did not exhibit any martensitic transformation even after cooling to −150 °C. Nonetheless, the present study provides fundamental information regarding the solute contents in the matrix after low temperature aging treatment. Transformable dispersion-strengthened alloys can then be designed using the phase relations obtained from these model alloys.

6. Conclusions

The precipitation of Ni_2TiAl Heusler phase in a TiNi based matrix has been investigated for Ni–Ti–Al and Ni–Ti–Al–X (X = Hf, Zr, Pd, Pt) alloys. The following conclusions are drawn:

1. Precipitation of Heusler phase Ni_2TiAl with $L2_1$-structure in a supersaturated $B2$–TiNi matrix is confirmed to form a coherent two-phase aggregate at the early stages. This is consistent with our motivating concept that the $B2$–$L2_1$ system, based on a bcc lattice, is directly analogous to the $A1$–$L1_2$ (fcc) system of γ′ precipitates in a γ matrix in Ni-based superalloys.
2. During isochronal aging for 1000 h, the microstructural dynamics of $L2_1$ precipitates in Ni–Ti–Al and Ni–Ti–Al–X (X = Hf, Zr) is governed by the growth process at 800 °C and by coarsening at 600 °C while kinetics in Ni–Ti–Al–X

(X = Pd, Pt) aged for 100 h can be explained by one process at both 600 and 800 °C.

3. For partitioning of Hf and Zr between $L2_1$ precipitates and the $B2$ matrix at 800 °C, the partitioning ratio is determined by AEM to be $\kappa_{Hf}^{B2/L2_1} = 2.17$ for Hf, and $\kappa_{Zr}^{B2/L2_1} = 1.35$ for Zr. At 600 °C, however, Hf and Zr show the inverse partitioning behavior, with values of 0.87 for Hf and 0.75 for Zr, as measured by 3DAP. The partitioning ratio of Pd at 800 °C is determined by 3DAP or AEM to be $\kappa_{Pd}^{B2/L2_1} = 0.64$ and 0.68 for 5 and 20 at.% substitution respectively, and $\kappa_{Pt}^{B2/L2_1} = 2.17$ for Pt. At 600 °C, $\kappa_{Pd}^{B2/L2_1} = 0.60$ and 0.53 for B + 5Pd and B + 20Pd, respectively.
4. The measured $B2$ lattice parameter of solution treated and quenched alloys, and the measured site occupancy of Hf and Zr in $B2$ at low temperature are consistent with the predictions from *ab initio* calculations.
5. The addition of Hf or Zr to the TiNi–Ni_2TiAl system at 800 °C is undesirable for lattice misfit reduction but useful for the control of martensite phase stability. At 600 °C, the partition behavior of Hf and Zr is effective for lattice misfit reduction. The addition of Pd is amenable for lattice misfit reduction at both 600 and 800 °C. On the other hand, Pt is undesirable for lattice misfit reduction at both temperatures but useful for the control of martensite phase stability.
6. The atomic volumes of Al, Hf, Ni, Pd, Pt, Ti, and Zr in TiNi and Ni_2TiAl are obtained based on lattice parameter measurements. Simple models to predict the lattice parameters of $B2$ and $L2_1$ phases are proposed for the control of lattice misfit in alloy design.
7. Key parameters have been established to support predictive design of nanodispersion-strengthened shape memory alloys for high-performance applications.

Acknowledgements

Financial support from the National Science Foundation (Grant No. DMR-9806749) and the Memry Corporation, Bethel, CT is gratefully acknowledged. The authors are also grateful to Dr. Dieter Isheim for his help with 3DAP experiments.

References

[1] Lin HC, Wu SK. Acta Metallurgica Et Materialia 1994;42:1623.
[2] Koizumi Y, Ro Y, Nakazawa S, Harada H. Materials Science and Engineering A 1997;223:36.
[3] Kajiwara S, Kikuchi T, Ogawa K, Matsunaga T, Miyazaki S. Philosophical Magazine Letters 1996;74:137.
[4] Kajiwara S. Journal De Physique IV 2001;11:395.
[5] Villars P, Calvert LD. Pearson's handbook of crystallographic data for intermetallic phases, 2nd ed. Newbury (OH): ASTM International; 1991.
[6] Johnson WC, Voorhees PW. Solid State Phenomena 1992;23:87.
[7] Sugimoto K, Kamei K, Sugimoto T, Sodeoka T. Effect of nickel and aluminum on internal friction in Ti–Ni and Ti–Ni–Al alloys. In: The International Conference on martensitic transformations. Nara, Japan: Japan Institute of Metals; 1986.
[8] Mulder JH, Maas JH, Beyer J. Martensitic transformations and shape memory effects in Ti–Ni–Zr alloys. In: International Conference on martensitic transformations. Monterey (CA): Monterey Institute for Advanced Studies; 1992.
[9] Angst DR, Thoma PE, Kao MY. Journal De Physique Iv 1995;5:747.
[10] Donkersloot HC, Van Vucht JH. Journal of the Less-Common Metals 1970;20:83.
[11] Lindquist PG. Structure and transformation behavior of martensitic titanium-(nickel, palladium) and titanium-(nickel, platinum) alloys. PhD thesis. University of Illinois at Urbana-Champaign, 1988 [p. 131].
[12] Kainuma R, Ohnuma I, Ishida K. Journal De Chimie Physique Et De Physico-Chimie Biologique 1997;94:978.
[13] Khalil-Allafi J, Dlouhy A, Eggeler G. Acta Materialia 2002;50:4255.
[14] http://rsb.info.nih.gov/nih-image/. NIH Image program. US National Institutes of Health: Bethesda (MD), 1999.
[15] Goldstein JI, Williams DB, Cliff G. Quantitative X-ray analysis. In: Joy DC, Romig Jr. AD, Goldstein JI, editors. Principles of analytical electron microscopy. NY: Plenum Press; 1986, p. 155.
[16] http://www.nist.gov/dtsa. Desktop spectrum analyzer. National Institute of Standards and Technology: Gaithersburg (MD), 1997.
[17] Jung J, Ghosh G, Isheim D, Olson GB. Metallurgical and Materials Transactions A 2003;34:1221.
[18] Horita Z, Sano T, Nemoto M. Journal of Microscopy-Oxford 1986;143:215.
[19] Williams DB. Practical analytical electron microscopy in materials science. Mahwah (NJ): Electron Optics Publishing Group; 1987.
[20] http://www.geol.uni-erlangen.de/macsoftware/macdiff/macdiff.html. MacDiff. Petschick R, 2000.
[21] International tables for crystallography. International Union of Crystallography. Kluwer Academic Publishers: Boston (MA), 1993; p. 65.

[22] Kresse G, Furthmuller J. Physical Review B 1996;54:11169.
[23] Kresse G, Furthmuller J. Computational Materials Science 1996;6:15.
[24] Vanderbilt D. Physical Review B 1990;41:7892.
[25] Methfessel M, Paxton AT. Physical Review B 1989;40:3616.
[26] Monkhorst HJ, Pack JD. Physical Review B 1976;13:5188.
[27] Shabalovskaya SA. International Materials Reviews 2001;46:233.
[28] Tang W, Sundman B, Sandstrom R, Qiu C. Acta Materialia 1999;47:3457.
[29] Ardell AJ, Nicholson RB. Acta Metallurgica 1966;14:1295.
[30] Su CH, Voorhees PW. Acta Materialia 1996;44:2001.
[31] Schmitz-Pranghe N, Dünner P. Zeitschrift Für Metallkunde 1968;59:377.
[32] Romans PA, Paasche OG, Kato H. Journal of the Less-Common Metals 1965;8:213.
[33] Schroder RH, Schmitz-Pranghe N, Kohlhaas R. Zeitschrift Fur Metallkunde 1972;63:12.
[34] German VN, Bakanova AA, Tarasova LA, Sumulov YN. Soviet Physics Solid State, USSR 1970;12:490.
[35] Rzyman K, Moser Z, Watson RE, Weinert M. Journal of Phase Equilibria 1998;19:106.
[36] Gachon JC, Selhaoui N, Aba B, Hertz J. Journal of Phase Equilibria 1992;13:506.
[37] Klopotov AA, Chekalkin TL, Gyunter VE. Technical Physics 2001;46:770.
[38] Hughes T, Lautenschlager EP, Cohen JB, Brittain JO. Journal of Applied Physics 1971;42:3705.
[39] Pasturel A, Colinet C, Manh DN, Paxton AT, vanSchilfgaarde M. Physical Review B 1995;52:15176.
[40] Fernando GW, Watson RE, Weinert M. Physical Review B 1992;45:8233.
[41] Mehrer H, Eggersmann M, Gude A, Salamon M, Sepiol B. Materials Science and Engineering A 1997;240:889.
[42] Huntington HB, Miller NC, Nerses V. Acta Metallurgica 1961;9:749.
[43] Gupta D, Lazarus D, Lieberman DS. Physical Review 1967;153:863.
[44] Gupta D, Lieberman DS. Physical Review B 1971;4:1070.
[45] Hahn H, Frohberg G, Wever H. Physica Status Solidi A 1983;79:559.
[46] Hancock GF, McDonnel Br. Physica Status Solidi A 1971;4:143.
[47] Minamino Y, Koizumi Y, Inui Y. Diffusion in B2-type ordered NiAl intermetallic compound. In: Diffusions in Materials: Dimat2000, Pts. 1 & 2. 2000 [p. 517].
[48] Donaldson AT, Rawlings RD. Acta Metallurgica 1976;24:285.
[49] Elcock EW, McCombie CW. Physical Review 1958;109:605.
[50] Bastin GF, Rieck GD. Metallurgical Transactions 1974;5:1827.
[51] Erdelyi G, Erdelyi Z, Beke DL, Bernardini J, Lexcellent C. Physical Review B 2000;62:11284.
[52] Bernardini J, Lexcellent C, Daroczi L, Beke D.L. Philosophical Magazine 2003;83:329.
[53] Langer JS, Schwartz AJ. Physical Review A 1980;21:948.
[54] Murch GE, Belova IV. Theory and simulation of diffusion kinetics in intermetallic compounds. In: Diffusion mechanisms in crystalline materials. San Francisco (CA): Materials Research Society; 1998.